



Developing superior catalysts engineered by multichannel healing strategy for advanced oxidation

Hong Xia^a, Zhen Zhang^a, Jia Liu^a, Xingming Ning^a, Shouting Zhang^a, Xiaoquan Lu^{a,b,*}

^a Tianjin Key Laboratory of Molecular Optoelectronic, Department of Chemistry, School of Science, Tianjin University, Tianjin, 300072, China

^b Key Laboratory of Bioelectrochemistry and Environmental Analysis of Gansu Province, College of Chemistry and Chemical Engineering, Northwest Normal University, Lanzhou, 730070, China



ARTICLE INFO

Keywords:

Multichannel-healing
Fe(III)/Fe(II) conversion
Hollow sandwich hybrid
Stability
Water treatment

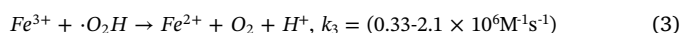
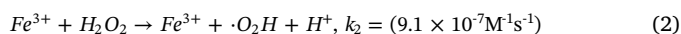
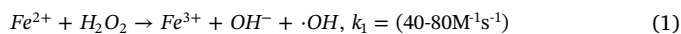
ABSTRACT

Catalyst deactivation derived from slow conversion of Fe(III)/Fe(II) is the critical problem restricting catalytic efficiency of advanced oxidation. Herein, a novel multichannel healing strategy is proposed for fast healing structural damage by designing rationally smart platform ($\text{TiO}_2\text{-CDs-FeOOH}$ hollow sandwich hybrid). This ingenious system shows remarkable catalytic activity (0.77 min^{-1}) and stability towards the removal of organic contaminants. Systematic studies confirm that the excellent catalytic activity is attributed to multiple electron transfer (MET) behavior at interface between photocatalytic substrate and FeOOH, leading to highly efficient interfacial charge separation and then fast recovery of Fe(II) on FeOOH surface during H_2O_2 activation process. Notably, multichannel healing procedure and MET kinetic information are unveiled by UV-vis/scanning electrochemical microscopy (SECM) through an *in situ* probe scanning technique. A higher ET rate constant k_{eff} ($0.92 \times 10^2 \text{ cm s}^{-1}$) was revealed over $\text{TiO}_2\text{-CDs-FeOOH}$, two times that of $\text{TiO}_2\text{-FeOOH}$, further confirming that multi-channel electron transfer could achieve fast Fe(III)/Fe(II) conversion. This work offers a new insight to design highly efficient catalysts for the practical applications of sustainable environmental remediation and energy conversion.

1. Introduction

Water pollution is one of the most severe global issues, which poses a pervasive threat to environment and human health [1–3]. Organic compounds are one of the most important groups of pollutants present in water, which are highly toxic, chemically stable and potentially carcinogenic. Thus, the development of powerful and practical treatments of organic compounds has attracted world-wide attention [4,5].

Advanced oxidation processes (AOPs) have been extensively employed in the removal of refractory organic pollutants in wastewater [6]. The conventional Fe^{2+} -based AOP involves the following equations:



Obviously, Eq. (2) determines the total efficiency of this reaction, of which the rate is still very low even assisted by co-catalysts. And due to

the high activity of Eq. (1) whereas low activity of Eq. (2), superfluous Fe^{3+} ions are generated, resulting in the formation of a mass of iron sludge [6,7]. Due to slow reduction of Fe(III), structural damage derived from rapid transformation of Fe(II) into inactive Fe(III) remains a major challenge and limits the Fe^{2+} -catalyzed AOPs performance. To address this issue, considerable efforts have been devoted to improving the Fe^{2+} -catalyzed AOPs [8]. For example, various materials were added as co-catalysts to accelerate Fe(III)/Fe(II) conversion. These reports mainly focused on the use of organic compounds, such as hydroxylamine, nitrilotriacetic acid, cysteine and so on, which worked as iron chelating agents or promoters to regulate the potential of Fe(III)/Fe(II) and facilitate the conversion of Fe(III) into Fe(II) [9–12]. Unfortunately, in these cases, it was hard to maintain stable catalytic activity owing to self-degradation of organic compounds induced by $\cdot\text{OH}$ [13]. Furthermore, organic matters can easily cause secondary pollution, making it very difficult to mineralize fully. Therefore, developing catalysts that can autonomously effectively heal and regenerate the structural damage without the use of any additional activator may be a promising approach. Recently, catalysis combined with solar energy

* Corresponding author at: Tianjin Key Laboratory of Molecular Optoelectronic, Department of Chemistry, School of Science, Tianjin University, Tianjin, 300072, China.

E-mail addresses: luxq@tju.edu.cn, luxq@nwnu.edu.cn (X. Lu).

has provided a fantastic route for sustainable energy conversion and environment treatment [14–17]. Light illumination has also been introduced into AOPs for promoting the AOPs performance. Some efforts have shown that the reduction of Fe^{3+} can be accelerated by accepting electrons from excited organic pollutants (e.g., various dyes) [18]. Besides, several studies have shown that the introduction of semiconductor materials (e.g., TiO_2 , BiVO_4) to Fenton system could enhance the degradation efficiency and promote $\text{Fe}(\text{III})/\text{Fe}(\text{II})$ conversion to a certain extent [19]. However, these reports mainly provided a single electron transfer pathway, namely transferring electrons from conduction band of semiconductor to $\text{Fe}(\text{III})$ species, which is incompetent to improve effectively charge separation and transport, leading to low conversion efficiency of $\text{Fe}(\text{III})/\text{Fe}(\text{II})$. Therefore, it is urgent to develop appropriate technologies for highly efficient chemical structure recovery. Multiple electron transfer is a promising strategy to promote charge separation of semiconductor, which makes it possible to develop a healing system via a meticulous design of hierarchical structure, aiming at synergistically accelerating charge carrier separation through multiple channels electron transfer, then achieving fast and effective healing of structural damage.

In this study, we proposed a new multichannel healing strategy by designing rationally hierarchical structure system ($\text{TiO}_2\text{-CDs-FeOOH}$). This ingenious system shows the improved catalytic activity and stability for the degradation of organic contaminants due to efficient interfacial charge separation and fast $\text{Fe}(\text{II})$ recovery via MET process. In addition, *in situ* SECM technology unveiled the multichannel healing procedure and the MET behavior, which found quantitative ET dynamic information of the different interfaces, providing some deep-seated synergic mechanism. A higher ET rate constant k_{eff} ($0.92 \times 10^{-2} \text{ cm s}^{-1}$) over $\text{TiO}_2\text{-CDs-FeOOH}$ further confirmed that multi-channel electron transfer could realize faster $\text{Fe}(\text{III})/\text{Fe}(\text{II})$ conversion compared to a single electron transfer pathway. This work not only offers a new insight to design highly efficient catalysts for the practical applications of environmental remediation and energy conversion, but also demonstrates a new approach to study catalytic procedure of light induced Fenton system.

2. Experimental methods

2.1. Synthesis of carbon dots (CDs)

The CDs were prepared by a hydrothermal method [20]. Typically, 1.0 g of urea and 3.0 g of citric acid were added to double-distilled water (10 mL) to form a transparent solution under stirring. The solution was then transferred to a 100 mL of Teflon-line autoclave for hydrothermal reaction at 180 °C for 5 h. The CDs solution was purified in a centrifuge to remove large or aggregated particles. Subsequently, the CDs solution was dried overnight at 70 °C to obtain CDs powder.

2.2. Synthesis of SiO_2 sphere and TiO_2 hollow spheres

SiO_2 spheres template was prepared by the Stöber method [16,21]. Briefly, 3.56 mL of aqueous ammonia ($\text{NH}_3\text{H}_2\text{O}$, 35%) and 10 mL of double-distilled water were added into 74.1 mL of absolute ethanol to from a mixture solution. Then, 5.6 mL of tetraethoxysilane (TEOS) was added into the above mixed solution and stirred for 14 h. The uniform SiO_2 spheres were obtained after washing with water and ethanol, respectively.

$\text{SiO}_2@\text{TiO}_2$ was synthesized through a typical hydrolysis and condensation of TBOT method [22]. 0.3 mL TBOT was mixed with 35 mL ethanol, 0.9 g SiO_2 spheres and 0.3 mL concentrated ammonia solution (28 wt%) under mechanical stirring. Then the solution was allowed to proceed for 24 h at 45 °C. The resulted product was centrifuged, washed with water and dried at 60 °C. Afterward, the powders were annealed in air at 550 °C for 2 h in muffle furnace to remove all organic compounds and crystallize the amorphous TiO_2 . The TiO_2 hollow spheres were

obtained by dissolving SiO_2 in NaOH (0.6 M) solution at 70 °C for 4 h. The final products were collected by centrifugation and washed with water several times. The as-prepared TiO_2 hollow spheres were neutralized with 1 M of HCl solution and then dried at 80 °C overnight.

2.3. Synthesis of $\text{TiO}_2\text{-CDs-FeOOH}$

To obtain ternary hierarchical $\text{TiO}_2\text{-CDs-FeOOH}$ hybrid material, 100 mg of as-obtained TiO_2 hollow spheres were dispersed in 30 mL of double-distilled water, then different amounts of CDs solution (0.5 mg mL^{-1}) was dropped into the suspension and stirring for 2 h at room temperature. Followed by adding a calculated amount of FeCl_3 into the above suspension with continuous stirring for another 2 h. The mixture was maintained at 80 °C for 12 h. The solid samples were centrifuged and washed with water to remove reactants. Finally, the obtained $\text{TiO}_2\text{-CDs-FeOOH}$ powders were dried at 40 °C in an oven. The samples were marked as $\text{TiO}_2\text{-}(x)\text{CDs-}(y)\text{FeOOH}$, where x, y represented mass fraction of CDs and FeOOH, respectively. For comparison, $\text{TiO}_2\text{-CDs}$ and $\text{TiO}_2\text{-FeOOH}$ were synthesized using the same procedure in the absence of FeCl_3 and CDs, respectively. FeOOH was synthesized using the same procedure in the absence of TiO_2 and CDs.

2.4. Materials characterizations

The X-ray diffraction (XRD) patterns of all samples were conducted over a Rigaku SmartLab (9 KW) diffractometer (Cu $\text{K}\alpha$ radiation, $\lambda = 1.5406 \text{ \AA}$) at settings of 40 kV and 50 mA. The X-ray photoelectron spectroscopy (XPS) signals were obtained with a Thermo Escalab 250xi system with an Al $\text{K}\alpha$ X-ray source (1486.6 eV). The binding energy was calibrated using the C1 s level at 284.6 eV as an internal standard. The morphologies and fine structures of samples were characterized by transmission electron microscopy (TEM) on a JEM-2100 F electron microscope operated at 200 kV. The surface morphologies were observed by field-emission scanning electron microscopy (FE-SEM) (Hitachi, SU8010). The UV-vis diffuse reflectance spectroscopy (UV-vis DRS) was recorded on a Shimadzu UV-3600 UV-vis-NIR spectrophotometer in the region of 200–800 nm with BaSO_4 as reflectance standard. Fourier transform infrared absorption spectroscopy (FT-IR) was performed with a BIO-RAD FTS 3000 spectrophotometer with the sample on a KBr wafer. Photoluminescence (PL) spectra was observed with a Hitachi F-7000 spectrometer under the 250 nm of excitation wavelength. Zeta potential of different samples was measured with a Malvern Nano-ZS90 zetasizer. Photoelectrochemical properties were measured by a CHI 920 electrochemical workstation with a standard three-electrode configuration in which catalyst-loaded ITO electrodes as working electrode, Pt foil as the counter electrode, and an Ag/AgCl electrode as the reference electrode under a Xe light irradiation in 0.1 M Na_2SO_4 solution. The introducing intensity-modulated photocurrent spectroscopy (IMPS) response was measured using the light source of a LED array (410 nm) driven by the output current of the Autolab LED Driver. Electrochemical impedance spectroscopy (EIS) analysis was performed on Autolab PGSTAT 302 (Metrohm, Switzerland) under a 410 nm LED light source. All the Nyquist plots of the samples were measured over a frequency range from 0.1 Hz to 10 kHz at open-circuit potential in 0.1 M Na_2SO_4 solution containing 0.1 M H_2O_2 . SECM measurements were carried out at a UV-vis/SECM platform proposed in the previous work [23,24]. Typically, a three-electrode setup was employed in the experiments. The SECM tip with 25 μm diameter ($\text{RG} = 3$, RG is the ratio of the overall electrode radius over the platinum disk radius) was employed as working electrode, a platinum wire served as auxiliary electrode, and an Ag/AgCl electrode served as the reference electrode. 1 mM $\text{K}_3\text{Fe}(\text{CN})_6$ in 0.1 M KCl and 1 mM trolamine (TEA, a hole scavenger) was used as probe molecule. The approach curves ($i_t\text{-}d$ curves) were obtained by moving the tip toward the interface between electrolyte and modified substrates and recording the tip current (i_t) as the function of the tip/interface separation distance (d). The k_{eff} can be

calculated from the experimental simulation [25].

2.5. Catalysis experiments

Catalytic performance of each sample was evaluated on the basis of the oxidation of tetracycline (TC) (10 mg L^{-1}) under light irradiation. All catalytic reactions were conducted in jacketed beaker with condensed water under constant stirring. A 300 W of Xenon lamp with wavelength cutoff filter ($\lambda \leq 420 \text{ nm}$) was used as the light source. The lamp was 10 cm away from the reaction solution. The pH value of solution was adjusted using the HCl or NaOH solution. Typically, 10 mg of $\text{TiO}_2\text{-CDs-FeOOH}$ powders was added into a beaker containing TC solution. Before irradiation, the suspension was stirred in dark for 60 min to achieve the adsorptive equilibrium between sample and TC. Then light-induced Fe^{2+} -catalyzed H_2O_2 decomposition process was started by adding a certain amount of H_2O_2 (30 wt%) to the solution. After a given time interval, 3 mL of analytical solution was taken out and immediately centrifuged before filtration through a $0.22 \mu\text{m}$ millipore filter to remove the catalysts. The filtrates were used to analyze the residual concentration of TC by recording the variations in the absorbance at 357 nm using a UV-vis spectroscopy. After each reaction, the solid catalyst was collected, washed with water, and dried to be reused in next cycle.

Trapping experiments were carried out in a similar experiment device as previously described for the catalytic degradation of TC. Different scavengers (1 mM) were added into the model pollution solution to trap holes (h^+), hydroxyl radicals (OH^-), electrons (e^-) and superoxide free radical (O_2^-), respectively.

The concentration of H_2O_2 was determined via titanium oxalate spectrophotometric method [19,26], which formed an orange complex (pertitanic acid) with a maximum absorption at 400 nm. The amount of total iron ions on samples and leached into the solution was detected with inductively coupled plasma-mass spectrometry (ICP-MS). The amount of ferrous on samples and the supernatant was measured at 510 nm by the iron-phenanthroline complex approach using a UV-vis spectroscopy [27].

Typically, in our catalytic system, the degradation kinetic data was fitted to the following first-order kinetics model [28]:

$$-\ln(C_t/C_0) = kt \quad (4)$$

Where C_t and k are the concentrations of TC and the rate constant at the time t , respectively.

3. Results and discussion

The $\text{TiO}_2\text{-CDs-FeOOH}$ composite was prepared by a hierarchical electrostatic assembly approach. The synthesis process and formation mechanism are shown in Fig. 1a. Surface charges play an important role in the formation of hierarchical structure, which can be estimated by measuring the zeta potentials (Table 1). First, TiO_2 hollow spheres were prepared by using SiO_2 spheres as sacrificial templates. Subsequently, TiO_2 hollow spheres were acidulated with 1 M of HCl solution (Fig. 1a-I). Then, the positively charged surface of TiO_2 ($\zeta = 16.7 \text{ mV}$) was absorbed by negatively charged CDs ($\zeta = -44.6 \text{ mV}$) to form $\text{TiO}_2\text{-CDs}$ ($\zeta = -35.9 \text{ mV}$) electrical bilayer (Fig. 1a-II). When FeCl_3 was added into the above mixture, the positively charged Fe^{3+} was attracted electrostatically to bridge negative charge (CDs) of the $\text{TiO}_2\text{-CDs}$, forming a positive-negative-positive electrical triple layer $\text{TiO}_2\text{-CDs-Fe}^{3+}$ ($\zeta = -19.2 \text{ mV}$) (Fig. 1a-III). CDs acted as a bridge to assemble two types of positively charged species, resulting in three materials being self-assembled together. After the hydrothermal process, Fe(III) was converted to FeOOH nanolayers, and CDs were embedded between the space of TiO_2 and FeOOH . The hierarchical $\text{TiO}_2\text{-CDs-FeOOH}$ hybrid material (Fig. 1a-IV) was finally obtained. CDs possess highly capturing and transport electron ability [29], which can be used as a bridge for electron transfer from TiO_2 to FeOOH .

The morphology of each step in synthesis process was characterized via SEM and TEM. As displayed in Fig. S1, TiO_2 showed hollow structure with a diameter of about 290 nm. After loading CDs and FeOOH , the composite still kept hollow structure (Fig. 1c), and the average size of spheres was almost unchanged ($\approx 290 \text{ nm}$), while it had a rougher surface due to the co-deposition of CDs and FeOOH (Fig. 1b). Seen from high resolution TEM (HRTEM) images (Fig. 2a), the average thickness of the shell was 20 nm. Fig. 2b demonstrated that thin CDs and FeOOH nanolayer with a total thickness of 10 nm has been compactly appended on the surface of TiO_2 shell. It could be observed from the partial enlarged view of Fig. 2b that a lattice spacing of 0.25 nm was indexed to the FeOOH (211) plane in the nanolayer, clearly suggesting a high crystallinity of FeOOH (Fig. 2c). The existence of CDs was shown in Fig. 2e. The measured lattice spacing was about 0.21 nm for CDs, which was matched well with graphitic carbon (101) planes [30,31]. Moreover, the lattice spacing of 0.352 nm was the characteristic lattice of TiO_2 (101) plane. The SAED pattern further confirmed the polycrystalline nature of the sample with distinct rings assigned to TiO_2 and FeOOH (Fig. 2d). To verify the entire distribution of each elements in the hollow spheres, the corresponding elemental mapping was characterized by using high angle annular dark field (HAADF) scanning transmission electron microscopy. As shown in Fig. 2g-l, the distribution of Ti, O, C, N and Fe elements was consistent with the morphology displayed in HAADF (Fig. 2g), which showed the homogenous distribution of CDs and FeOOH over the whole sphere. It also implied the good loading and high dispersion of CDs and FeOOH in TiO_2 sphere.

The chemical composition of $\text{TiO}_2\text{-CDs-FeOOH}$ was confirmed by XRD patterns and FT-IR spectrum (Fig. 3). As shown in Fig. 3a, all the characteristic peaks could be indexed to anatase TiO_2 (JCPDS No. 21-1272). After loading of CDs and FeOOH , no peaks ascribed to CDs and FeOOH were observed in XRD patterns due to their low concentration (the loading of CDs and Fe was both 5 wt%). The XRD patterns for pure CDs and FeOOH were shown in Fig. S2. The FT-IR spectra of $\text{TiO}_2\text{-CDs-FeOOH}$ was shown in Fig. 3b. Compared with TiO_2 , some new absorption peaks could be observed. The bands located at 2922, 2855 and 1390 cm^{-1} were ascribed to C–H stretching vibration of methylene ($-\text{CH}_2-$) and methine (CH) and skeletal vibration of symmetric carboxylate (C=O), respectively, which were in accord with the characteristic absorption peaks of CDs [20,32]. Besides, the weak peak at 670 cm^{-1} was attributed to the vibration of Fe–O bonding originating from the formation of FeOOH [33]. The XRD and FT-IR results further proved the successful preparation of $\text{TiO}_2\text{-CDs-FeOOH}$ composite.

Elements construction and valence status of $\text{TiO}_2\text{-CDs-FeOOH}$ were investigated by XPS. As expected, the full scan spectrum showed the existence of Ti, O, Fe and C elements in the sample (Fig. 3c). The two peaks of high resolution Ti 2p spectrum at 459.0 eV ($\text{Ti } 2\text{p}_{3/2}$) and 464.7 eV ($\text{Ti } 2\text{p}_{1/2}$), together with the peak of high resolution O 1s region at 530.5 eV were certified as typical characteristic peaks of TiO_2 (Figs. 3d and S3) [34–36]. High resolution C1s spectra fitted into several C species with different binding energy, which were attributed to C–C, C–N, C–O and C = O, respectively (Fig. 3e). The above results indicated that CDs were loaded on the surface of TiO_2 [35]. Fig. 3f demonstrated that the element Fe mainly existed as FeOOH [15,37]. The Fe 2p_{3/2} and 2p_{1/2} peaks could be deconvoluted into three peaks, respectively, including 710.8 eV and 724.2 eV for Fe^{2+} , 712.8 and 728.4 eV for Fe^{3+} , and 717.6 and 730.4 eV for satellite peak, which confirmed the coexistence of Fe^{3+} and Fe^{2+} in $\text{TiO}_2\text{-CDs-FeOOH}$.

The catalytic activities of the hierarchical $\text{TiO}_2\text{-CDs-FeOOH}$ were evaluated by TC degradation under light irradiation. When the loading amount of FeOOH was lower than 5%, the ternary composite exhibited a higher photocatalytic degradation than $\text{TiO}_2\text{-CDs}$, FeOOH or $\text{TiO}_2\text{-FeOOH}$ (Fig. 4a). The degradation kinetic is fitted well to pseudo-first-order kinetics in all cases. The rate constant (k) of $8.62 \times 10^{-2} \text{ min}^{-1}$ was calculated for $\text{TiO}_2\text{-CDs-FeOOH}$ (5%), which was greater than the values of $3.12 \times 10^{-2} \text{ min}^{-1}$, $3.24 \times 10^{-2} \text{ min}^{-1}$ and $3.19 \times 10^{-2} \text{ min}^{-1}$ obtained from $\text{TiO}_2\text{-CDs}$, FeOOH and $\text{TiO}_2\text{-FeOOH}$. When only H_2O_2

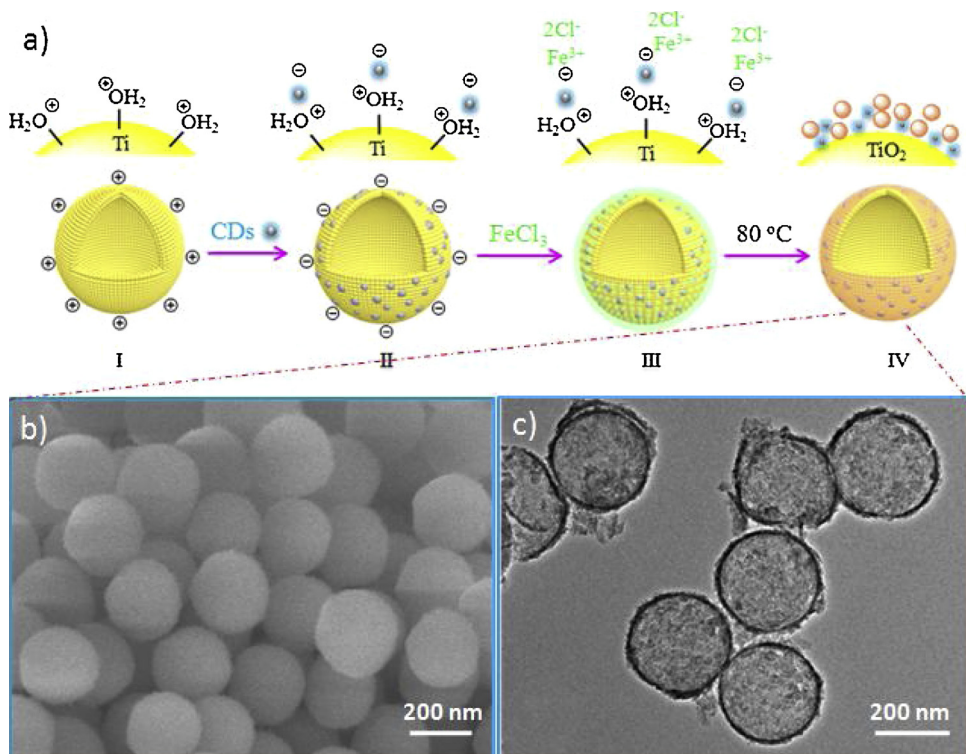


Fig. 1. (a) Illustrating of the positive-negative-positive hierarchical electrostatic assembly synthesis process for $\text{TiO}_2\text{-CDs-FeOOH}$ hierarchical nanohybrid, (b) SEM and (c) TEM images of $\text{TiO}_2\text{-CDs-FeOOH}$.

Table 1

Zeta potentials of TiO_2 hollow spheres, $\text{TiO}_2\text{-CDs}$, $\text{TiO}_2\text{-CDs-Fe}^{3+}$ and CDs.

Sample	TiO_2 hollow spheres	acid-treated TiO_2	$\text{TiO}_2\text{-CDs}$	$\text{TiO}_2\text{-CDs-Fe}^{3+}$	CDs
Zeta potential (mV)	-4.5	16.7	-35.9	-19.2	-44.6

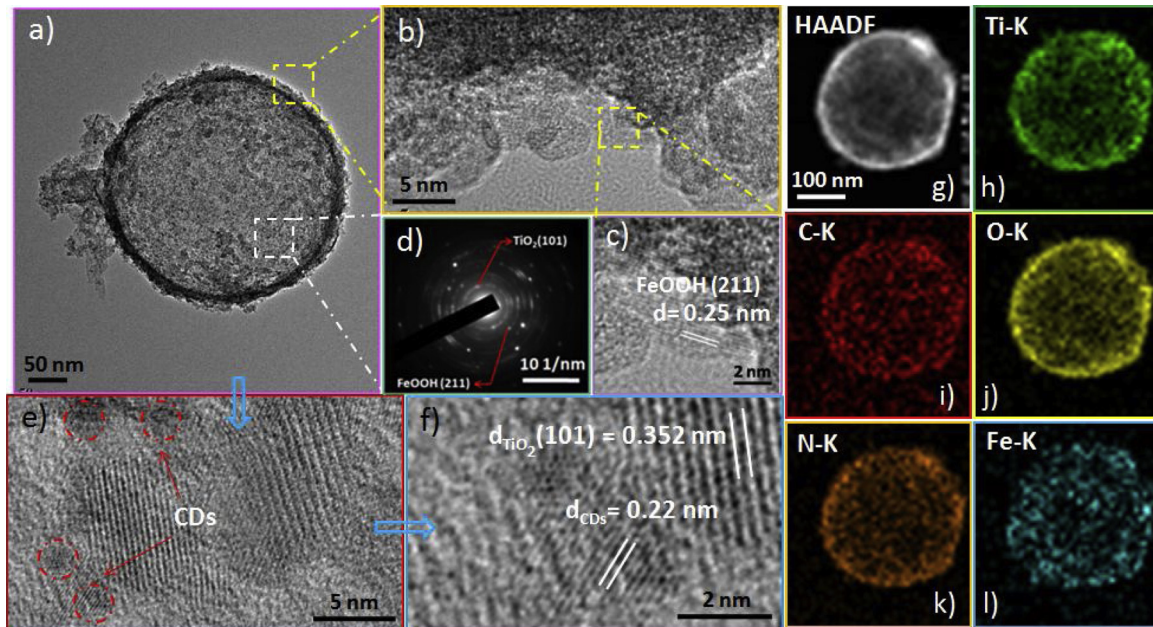


Fig. 2. (a–f) HRTEM images and SAED pattern of $\text{TiO}_2\text{-CDs-FeOOH}$ hollow sphere, (g–l) STEM image and corresponding element mapping images of $\text{TiO}_2\text{-CDs-FeOOH}$.

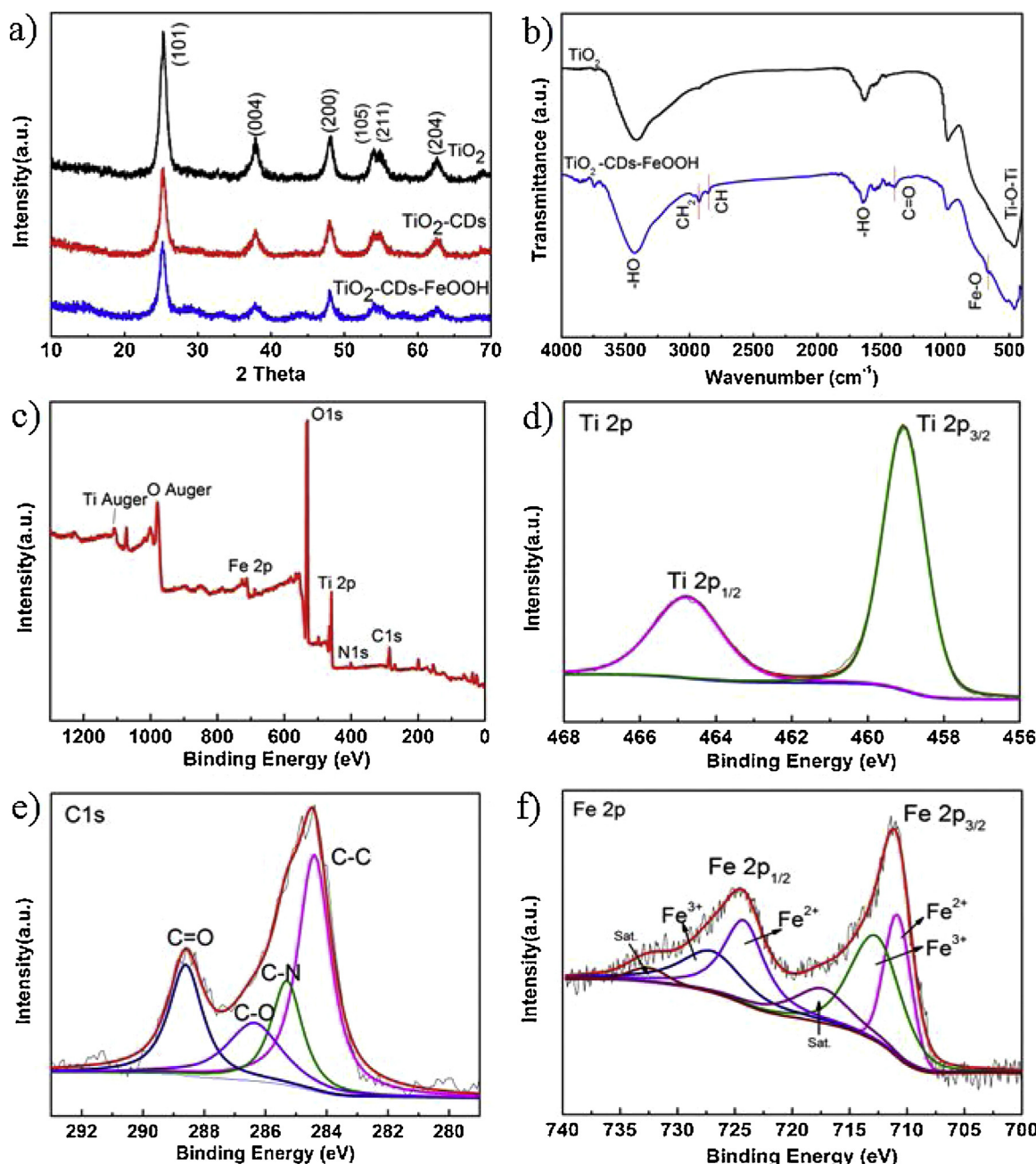


Fig. 3. (a) XRD patterns, (b) FT-IR spectra of TiO_2 and $\text{TiO}_2\text{-CDs-FeOOH}$, (c) full XPS spectrum of $\text{TiO}_2\text{-CDs-FeOOH}$, (d) Ti 2p, (e) C1s and (f) Fe 2p XPS spectra.

was added to the system, about 42% of TC was removed in 60 min over $\text{TiO}_2\text{-CDs}$, which was mainly derived from the absorption toward TC. With the increase of the loading amount of FeOOH, TC degradation rates increased from $1.75 \times 10^{-3} \text{ min}^{-1}$ to $6.29 \times 10^{-2} \text{ min}^{-1}$. Pure FeOOH exhibited the best catalytic performance with a rate constant of $7.07 \times 10^{-2} \text{ min}^{-1}$ (Fig. 4d). In the co-existence of H_2O_2 and light irradiation (Fig. 5), degradation rate of $9.63 \times 10^{-2} \text{ min}^{-1}$ was obtained for $\text{TiO}_2\text{-CDs}$, indicating that the excited electron-hole pairs could facilitate H_2O_2 activation to some extent. Compared with Fenton oxidation, the light induced Fenton system using FeOOH showed a similar TC degradation ability, giving a degradation rate of $8.04 \times 10^{-2} \text{ min}^{-1}$. Interestingly, after integrating with the $\text{TiO}_2\text{-CDs}$ hollow sphere, TC degradation rate was dramatically enhanced. TC was completely catalytically decomposed within 3 min using $\text{TiO}_2\text{-CDs-FeOOH}$ (5%) with a rate constant of $7.72 \times 10^{-1} \text{ min}^{-1}$, which correspond to an increase of almost ten times compared with that using photo- or Fenton-oxidation

alone. Moreover, it was more than two and a half times greater than $\text{TiO}_2\text{-FeOOH}$. The catalytic rate was superior to those of the Fe-based catalysts reported elsewhere [19]. A further increase in the amount of FeOOH inhibited the enhancement in degradation rate. The contribution of homogeneous Fenton catalysis can be neglected due to the negligible iron leaching concentration in solution (The concentration of leached iron (0.028 mg L^{-1}) was detected by ICP-MS). The above results implied that photo-oxidation and Fe^{2+} -catalyzed H_2O_2 oxidation were mutually reinforced, and the ternary composites exhibited higher activity compared to bare FeOOH and other binary composites. In addition, this hierarchical $\text{TiO}_2\text{-CDs-FeOOH}$ exhibited high TC degradation efficiency even at high pH values, demonstrating a wide pH working range of this smart platform (Fig. 5c). Catalytic stability is an important factor, so the stability of $\text{TiO}_2\text{-CDs-FeOOH}$ for AOPs was examined by carrying out a test over five cycles (Fig. 5d), and it maintained almost the same activity level after five cycles. Moreover, low iron leaching

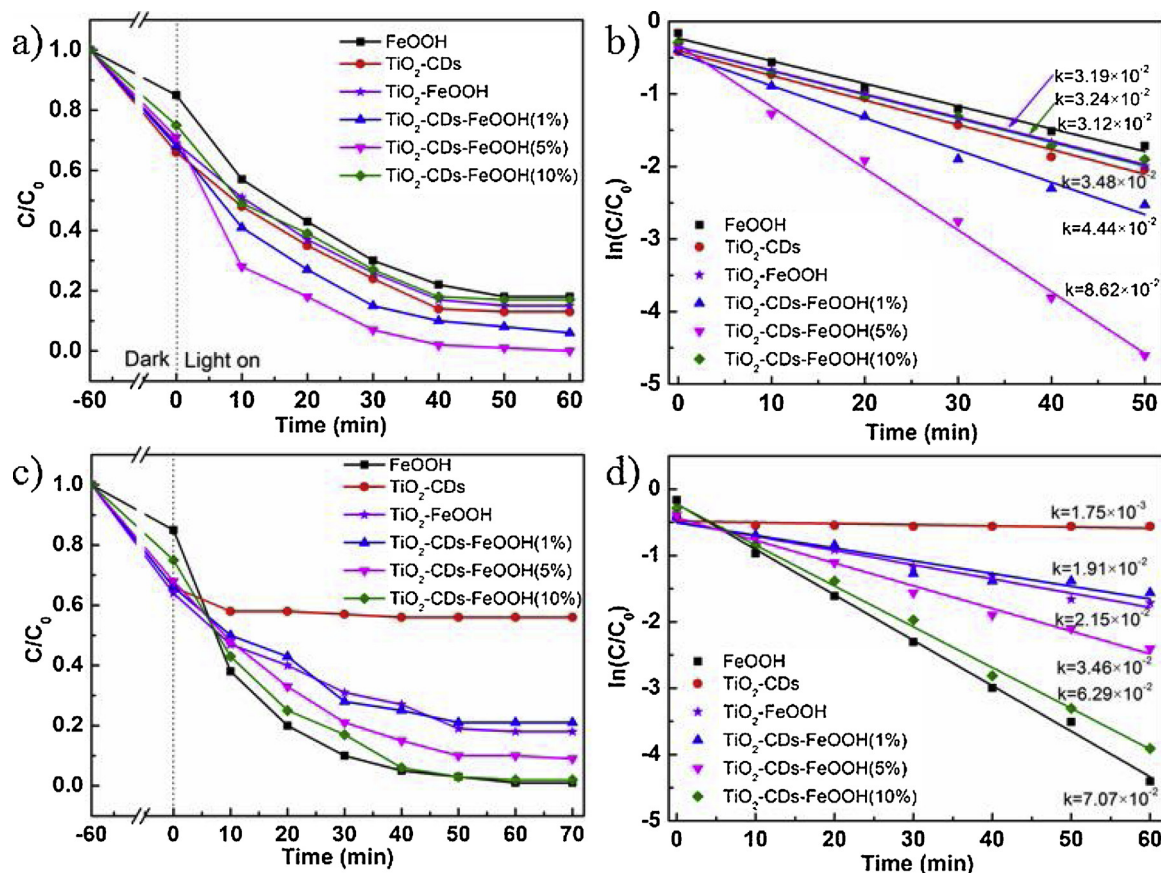


Fig. 4. (a) photocatalytic degradation of TC, (b) Fe^{2+} -catalyzed H_2O_2 activation for TC degradation in the presence of different catalysts. The loading of CDs is 5 wt %.

concentration (0.099 mg L^{-1}) was detected, indicating that TiO_2 -CDs-FeOOH had good stability.

To gain deep insights into this catalytic process, trapping experiments were carried out. Various scavenger agents such as tertbutyl alcohol (TBA), 1,4-benzoquinone (BQ), AgNO_3 and ammonium oxalate (AO) were selected to trap $\cdot\text{OH}$, $\cdot\text{O}_2^-$, e^- and h^+ , respectively [17,22,28]. As displayed in Fig. 6, the addition of BQ has almost no effect on the degradation of TC, which indicated that $\cdot\text{O}_2^-$ was not responsible for TC degradation. Because of the more positive position of E_{CB} of TiO_2 (-0.29 eV) than $\text{O}_2/\cdot\text{O}_2^-$ potential (-0.33 eV), the photo-generated electron could not reduce the adsorbed O_2 to produce $\cdot\text{O}_2^-$. In the presence of AO, the degradation rate slightly decreased, revealing that h^+ was involved in this reaction system. Moreover, when TBA or AgNO_3 was present, this degradation process was significantly restrained, with inhibition rates of 55% and 40%, respectively. These results indicated that $\cdot\text{OH}$ and e^- acted main parts in TC degradation. Considering weak direct photolysis of H_2O_2 (Fig. 4c), an amount of $\cdot\text{OH}$ might be generated by Fe^{2+} -catalyzed H_2O_2 activation process ($\text{Fe}^{2+} + \text{H}_2\text{O}_2 \rightarrow \cdot\text{OH} + \text{Fe}^{3+} + \text{OH}^-$) and photo-oxidation of adsorbed H_2O or OH^- by holes of TiO_2 ($\text{H}_2\text{O}/\text{OH}^- + \text{h}^+ \rightarrow \cdot\text{OH} + \text{H}^+$). As for electrons, they could not reduce O_2 to produce $\cdot\text{O}_2^-$. However, they could influence this system via transferring to the surface-grafted $\text{Fe}(\text{III})$ species to trigger reduction reaction then activate H_2O_2 . This observation was in accord with those reported previously [19,22].

Whereafter, a series of comparative characterization were carried out to elucidate coupling mechanism between different photocatalyst substrates and Fe^{2+} -catalyzed H_2O_2 activation. Optical behavior of all the samples was investigated using UV-vis diffuse reflectance spectroscopy (UV-vis DRS). As shown in Fig. 7a, the wavelength of TiO_2 absorption edge was located at 390 nm, which was in accordance with the band gap energy of 3.2 eV for anatase TiO_2 [38]. After loading of

FeOOH , TiO_2 -FeOOH showed an enhanced absorption in the visible light owing to the grafting of $\text{Fe}(\text{III})$ species as visible-light absorbers [39,40]. As for TiO_2 -CDs sample, it gave a better light response than pure TiO_2 due to the deposition of CDs that are excellent visible-light photosensitizers and can promote efficiently light harvesting [41,42]. After further loading FeOOH on the surface of TiO_2 -CDs, there was a strong and broad absorption peak covering the whole visible light region. The TiO_2 -CDs-FeOOH composite exhibited a more outstanding optical property, which was beneficial to improve photocatalytic efficiency. Photoluminescence and photoelectrochemical study were performed to investigate charge separation and migration. It was found that the emission position was not much changed after introducing CDs and FeOOH , but the emission intensity significantly decreased. The PL intensity followed the order TiO_2 -CDs-FeOOH < TiO_2 -CDs < TiO_2 -FeOOH < TiO_2 . TiO_2 -CDs-FeOOH had the lowest PL intensity among all the catalysts (Fig. 7b), which illustrated a fact that CDs and surface-grafted $\text{Fe}(\text{III})$ species could both promote charge separation of TiO_2 , and the coexistence of them resulted in the highest separation efficiency. Owing to the band position of CDs, it allows electron transfer from the surface of excited TiO_2 under UV irradiation [29,42]. Surface-grafted $\text{Fe}(\text{III})$ can trap the photoelectrons of TiO_2 by interfacial charge transfer (IFCT) due to good match with the potential of $\text{Fe}^{3+}/\text{Fe}^{2+}$ redox couple (0.77 V) [39,40]. TiO_2 -CDs-FeOOH exhibited the best charge separation ability because of two electron migration paths, namely partial electrons injected to CDs then to FeOOH and another parts migrated directly to $\text{Fe}(\text{III})$ species. The transfer efficiency of charge of TiO_2 -CDs-FeOOH, TiO_2 -CDs, TiO_2 -FeOOH and bare TiO_2 was measured in 0.1 M Na_2SO_4 solution. Fig. 7c showed the photocurrent responses in dark and light conditions. As expected, the ternary composite (TiO_2 -CDs-FeOOH) showed the highest photocurrent intensity, indicating that loading of CDs and FeOOH not only can boost the charge

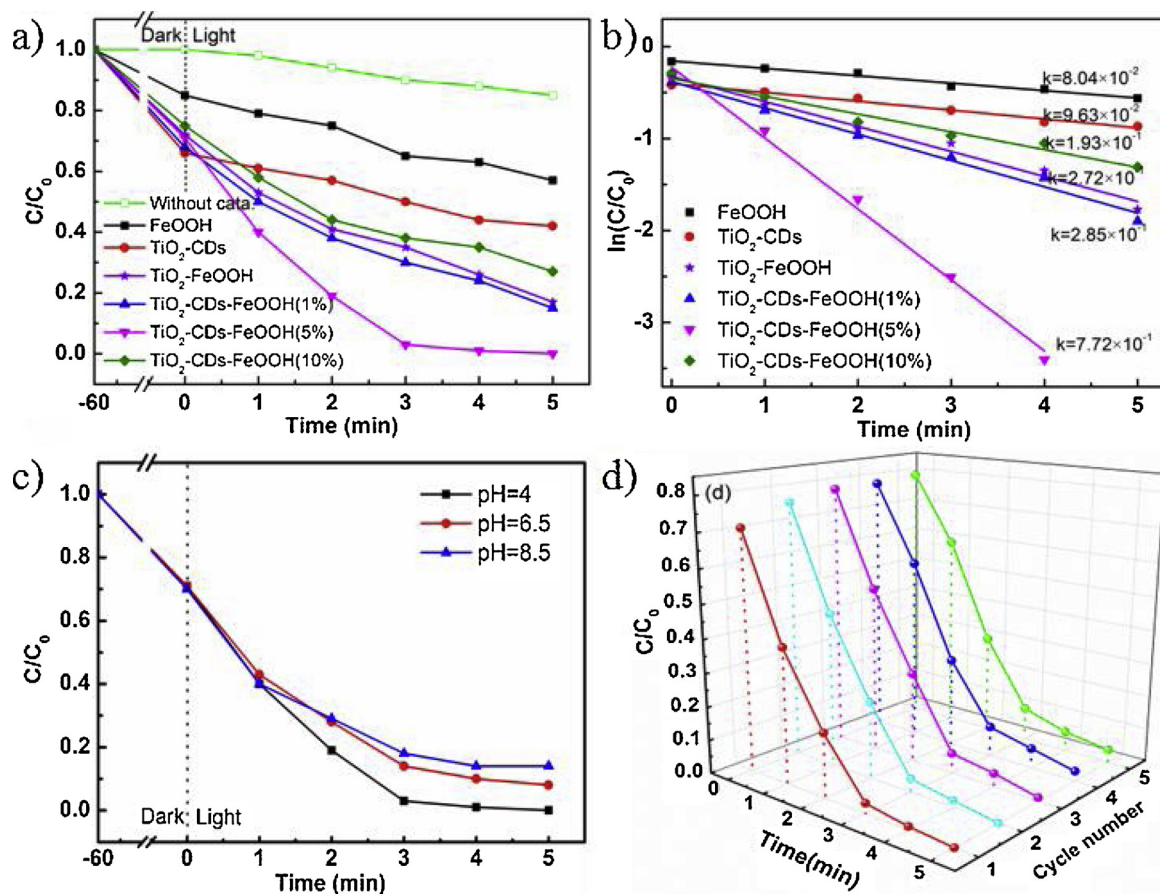


Fig. 5. (a) light induced Fe^{2+} -catalyzed H_2O_2 activation for TC degradation in the presence of different catalysts at pH 4, (b) corresponding degradation kinetic of TC, (c) effect of pH on TC degradation, (d) cycling test of the catalytic performance of light induced H_2O_2 activation using TiO_2 -CDs-FeOOH (5%). The loading of CDs is 5 wt%.

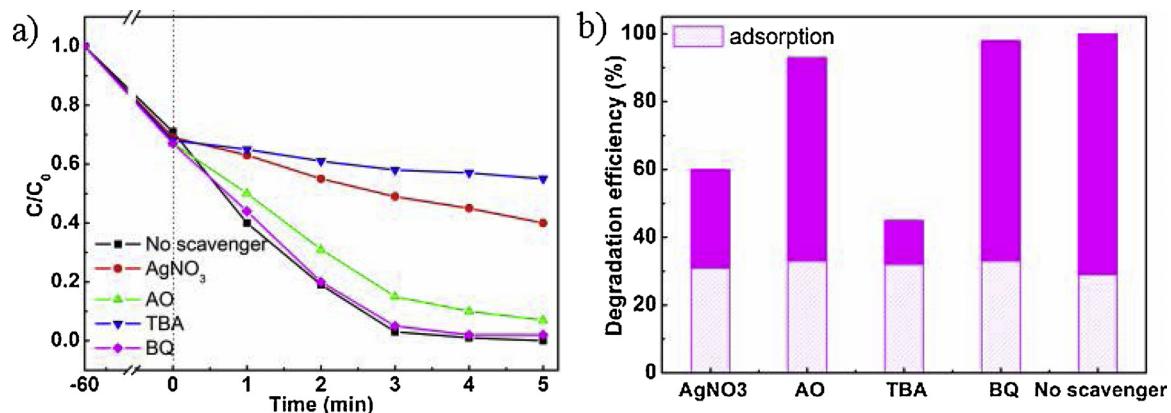


Fig. 6. (a) Controlled experiments using different scavengers (1 mM) for the degradation of TC, (b) corresponding degradation efficiency in the presence of different scavengers.

separation but also can accelerate release and transfer them. The charge carrier dynamics were analyzed by IMPS. The average transport time τ of photoexcited electrons to diffuse to the electrode can be estimated by Eq. (5) [43]:

$$\tau = 1/(2\pi f_{\text{IMPS}}) \quad (5)$$

where f_{IMPS} is the frequency at which the minimum in the IMPS plot occurs. As shown in Fig. 7d, the electron-transport time for FeOOH, TiO_2 -FeOOH and TiO_2 -CDs-FeOOH was calculated to be 0.44, 0.30 and 0.25 ms, respectively. TiO_2 -CDs-FeOOH hybrid showed the shortest τ value compared to other samples, indicating more facile transfer of

photoexcited electrons across interface between TiO_2 , CDs and FeOOH as well as lower recombination sites in TiO_2 -CDs-FeOOH hybrid. Because of the embedding of CDs in the space of TiO_2 and FeOOH, the faster charge transport is likely due to that graphite carbon can induce expediently electron-hole pair separation and facilitate charge shuttling between TiO_2 and FeOOH surface, allowing the electrons with longer lifetime to be collected swiftly. In addition, because the catalytic reaction was taken place in solution containing H_2O_2 , the charge transfer properties at interface between catalysts solid and H_2O_2 was further evaluated by means of EIS measurements (Fig. 7e and f). As reflected by its smaller impedance arc radius, the electrical resistance of FeOOH was

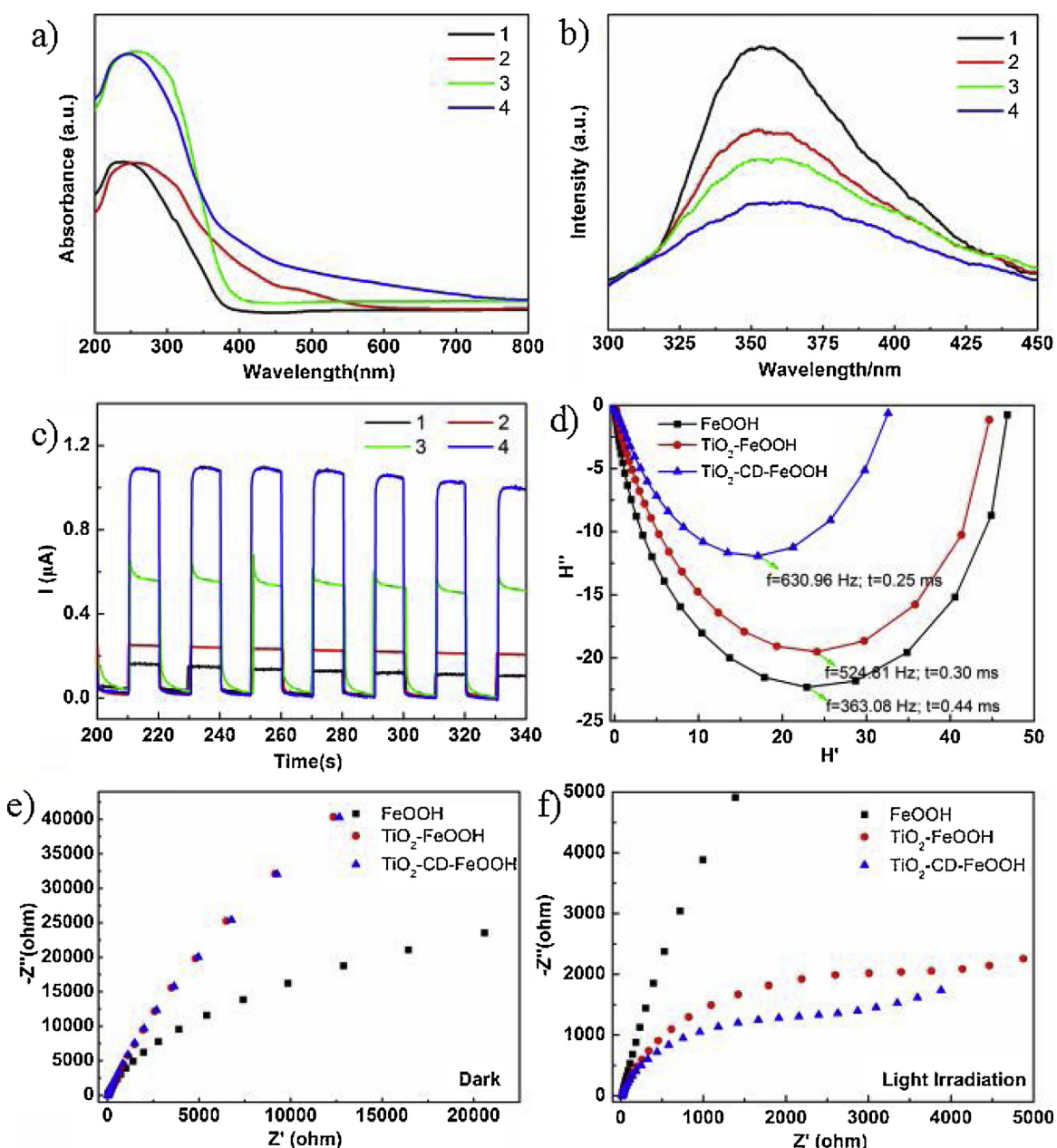


Fig. 7. (a) UV-vis diffuse reflectance spectra, (b) PL emission spectra (the excitation wavelength is 250 nm) and (c) transient photocurrent performance of 1) TiO_2 , 2) TiO_2 -FeOOH, 3) TiO_2 -CD and 4) TiO_2 -CD-FeOOH, (d) IMPS measured in 0.1 M Na_2SO_4 solution containing 0.1 M H_2O_2 with light irradiation, (e) EIS Nyquist plots in the dark and (f) with light irradiation. The loading of CDs and FeOOH is both 5 wt %.

smaller than that of FeOOH-based hybrids in the dark, which was undoubtedly attributed to the efficient activation of H_2O_2 through the Fe sites (Fig. 7e). Under light illumination, smaller charge transfer resistance was measured on the three electrodes due to their photoactive properties [44]. Obviously, TiO_2 -CDs-FeOOH exhibited the lowest charge transfer resistance, implying a faster surface reaction due to the enhanced photogenerated electron-hole separation efficiency or incremental activation of H_2O_2 through the surface-grafted Fe sites (Fig. 7f).

In principle, Fe(II) in Fenton process is unstable and easily transformed into Fe(III), thereby gradually lowering the H_2O_2 activation efficacy. To verify the effect of different substrates (e.g., TiO_2 , TiO_2 -CDs) on surface Fe species, chemical state changes of Fe species after excitation were investigated by determining the concentration of Fe(II) on the surface of catalyst during the reaction. As shown in Fig. 8a, the reduction behavior was discovered on all catalysts in the absence of H_2O_2 under light irradiation. Notably, the Fe^{2+} concentration on TiO_2 -

FeOOH was two times higher than that on pure FeOOH, indicating that photoelectrons derived from TiO_2 can facilitate the reduction of surface-grafted Fe(III) species. After embedding CDs in TiO_2 -FeOOH, Fe^{2+} concentration increased further. In addition to direct reduction by photoelectrons of TiO_2 , CDs, an excellent electron acceptor and donor [32], can trap electrons from semiconductor TiO_2 and then donate them to subsequent reduction reaction under UV irradiation. Moreover, CDs embedded the space between TiO_2 and FeOOH, and this intimate interfacial contact could lead to that photoexcited electrons were much easier to be transferred and trapped by FeOOH. CDs serve as an effective electron enrichment and transport layer, which promotes the utilization and transportation of photoelectrons, thus leading to higher photoreduction efficiency. As for all catalyst, there was a similar trend that the Fe^{2+} concentration on catalyst increased dramatically over 10 min and then decreased slightly with time. When a certain amount of H_2O_2 was added, Fe^{2+} concentration significantly decreased compared

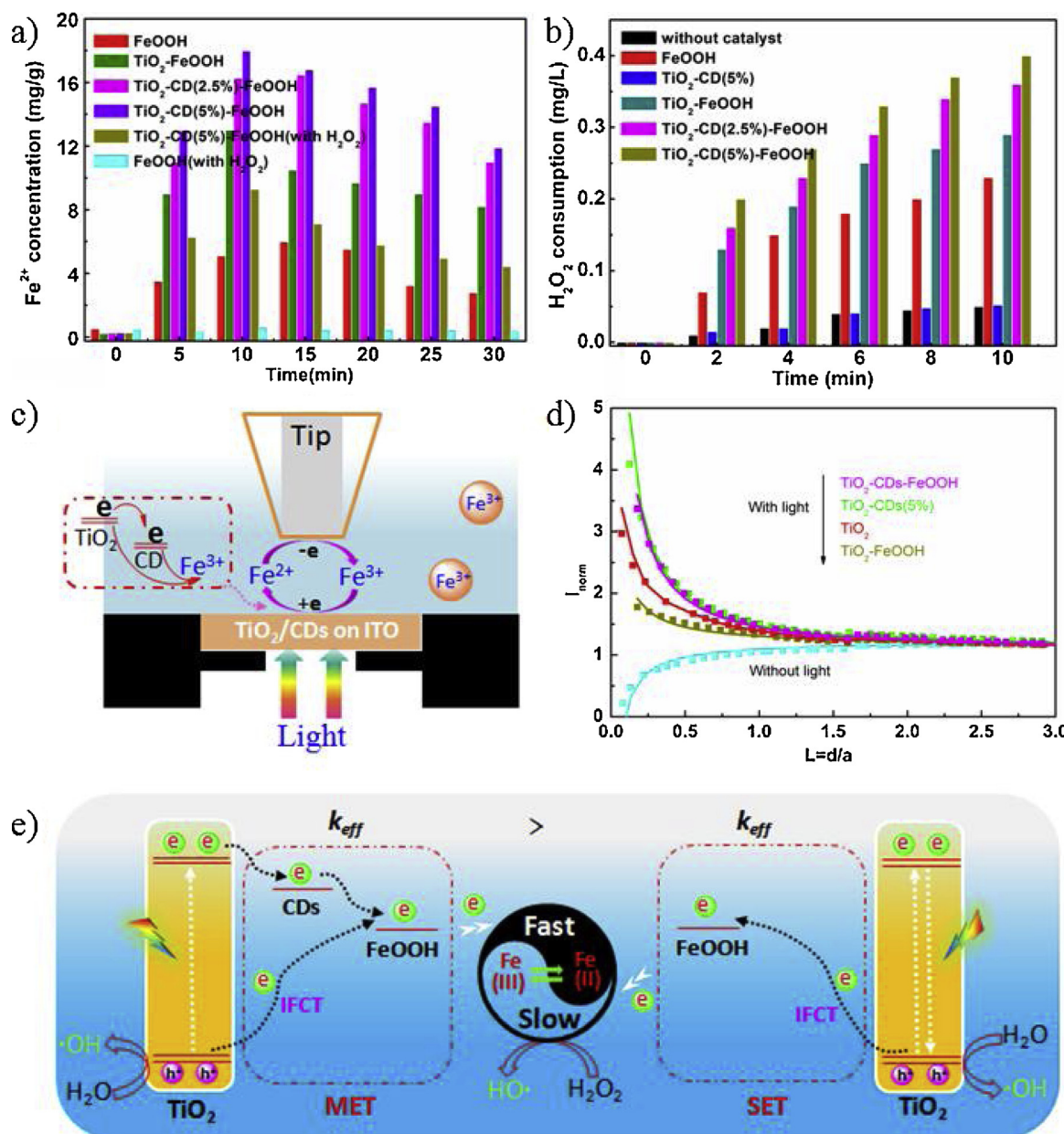


Fig. 8. (a) Fe^{2+} concentration on the catalysts in the presence and absence of H_2O_2 under light irradiation, (b) corresponding H_2O_2 consumption over different catalysts, the loading of FeOOH in all catalysts is 5 wt%, (c) schematic illustration of testing process using SECM, (d) probe approach curves of different modified substrates (TiO_2 , $\text{TiO}_2\text{-FeOOH}$, $\text{TiO}_2\text{-CDs}$ and $\text{TiO}_2\text{-CDs-FeOOH}$), $E_{\text{tip}} = 0.3 \text{ V}$ versus Ag/AgCl . (e) illustration of multi-channel charge transfer over $\text{TiO}_2\text{-CDs-FeOOH}$.

Table 2

Heterogeneous electron transfer rate constant (k_{eff}) of TiO_2 , $\text{TiO}_2\text{-CDs}$ and $\text{TiO}_2\text{-CDs-FeOOH}$ under light irradiation. D: The diffusion coefficient of $\text{K}_3\text{Fe}(\text{CN})_6$ ($1.75 \times 10^{-5} \text{ cm}^2 \text{ s}^{-1}$).

Sample	TiO_2 spheres	$\text{TiO}_2\text{-FeOOH}$	$\text{TiO}_2\text{-CDs}$ (5%)	$\text{TiO}_2\text{-CDs-FeOOH}$
k_{eff} ($10^{-2} \text{ cm s}^{-1}$)	0.51	0.48	0.99	0.92

with that in absence of H_2O_2 . This implied that the generated Fe^{2+} could quickly react with H_2O_2 . Upon lack of H_2O_2 , the generated Fe^{2+} was relatively long-lived and accumulated on the catalysts. The slight decrease in Fe^{2+} concentration with time in the absence of H_2O_2 may be due to in situ formation of a small amount of H_2O_2 during degradation progress. Fe^{2+} concentration on $\text{TiO}_2\text{-CDs-FeOOH}$ is much higher than that on FeOOH or TiO_2 , indicating that CDs play an

important role in greatly accelerating $\text{Fe}(\text{II})$ recovery. This stimulative behavior is due to multi-channel electron transfer, leading to more efficient charge separation and photoreduction efficiency.

It is well known that accelerated $\text{Fe}(\text{III})/\text{Fe}(\text{II})$ conversion will lead to an enhancement in H_2O_2 consumption. Fig. 8b depicted the consumption of H_2O_2 over different catalysts under light irradiation. With only light irradiation, H_2O_2 did not exhibit significant consumption, suggesting weak direct photolysis of H_2O_2 . This was consistent with the above results (Fig. 5a). Compared with pure FeOOH and $\text{TiO}_2\text{-FeOOH}$, $\text{TiO}_2\text{-CDs-FeOOH}$ composite greatly enhanced the H_2O_2 consumption, and showed a continuous increase when the CDs content was increased from 0% to 5%. However, Fig. 8b showed that no obvious increase in H_2O_2 consumption over $\text{TiO}_2\text{-CDs}$ was observed compared to that in the absence of catalyst, implying that photoelectrons and holes contributed very small to the enhanced H_2O_2 consumption. Hence, accelerated $\text{Fe}(\text{III})/\text{Fe}(\text{II})$ conversion leads to higher H_2O_2 consumption, which is in accord with the result of chemical state changes of Fe species.

Although the introduction of semiconductor materials to Fenton system can promote Fe(III)/Fe(II) conversion, we are poorly aware of the concrete electron transfer procedure in such systems. Hence, to confirm these doubtful points and prove the effect of multi-channel electron transfer on Fe(II) recovery, UV-vis/SECM as a powerful in situ electrochemical technique has been used to quantize directly the kinetic information of multi-channel electron transfer at different surfaces including TiO₂, TiO₂-FeOOH, TiO₂-CDs and TiO₂-CDs-FeOOH. In SECM measurement process, [Fe(CN)₆]³⁻ was chosen as probe molecule, and meanwhile it can simulate the role of Fe(III) in TiO₂-FeOOH or TiO₂-CDs-FeOOH (Fig. 8c). When the tip approached the substrate under light illumination, "positive feedback" approach curve was seen. On the contrary, "negative feedback" curve was observed in the dark condition (Fig. 8d). The positive feedback behavior was because of an increasing probe current derived from the regeneration of Fe(III) at the tip. This indicated the occurrence of a rapid photoelectrons transfer between Fe(III) and substrate materials on ITO. Compared to TiO₂, TiO₂-CDs showed higher positive feedback current (Fig. 8d). Coupled with data fitting, quantitative kinetic rate constants (k_{eff}) of different interfaces can be obtained, as shown in Table 2. TiO₂-CDs showed a higher electrons transfer rate constant ($0.99 \times 10^{-2} \text{ cm s}^{-1}$), which was about two times higher than that of TiO₂, reflecting that CDs could facilitate the migration of photoelectrons. Nevertheless, after integrating with FeOOH, electron transfer rate constant k_{eff} followed an order of TiO₂-CDs (5%) > TiO₂-CDs-FeOOH > TiO₂ spheres > TiO₂-FeOOH. TiO₂-CDs-FeOOH and TiO₂-FeOOH substrates exhibited slightly lower tip current compared with TiO₂-CDs (5%) and TiO₂ spheres, respectively, which indicated that photoelectrons were partially captured by the surface-grafted Fe(III), leading to decreasing tip current and electron transfer rate constants. Moreover, k_{eff} of TiO₂-CDs-FeOOH exhibited nearly twice as high as TiO₂-FeOOH, further confirming that multiple channels electron transfer could effectively increase the reduction of surface-grafted Fe(III) species. The above SECM results inspire us that the rationally designed electron transfer system is more favorable for catalytic efficiency and chemical structure recovery.

Based on the above discussion, the catalytic process on account of multiple channels electron transfer and Fe(II) recovery was illustrated in Fig. 8e. Under light irradiation, the electrons and holes were motivated from TiO₂ shells. And then the hole was accumulated at the surface of TiO₂, which was apt to oxidize adsorbed H₂O or OH⁻. Meanwhile, electrons transferred from TiO₂ to FeOOH by two channels, namely, partial electrons were injected from TiO₂ to CDs and then to FeOOH, and another part was injected from TiO₂ to FeOOH directly. The multiple-channels migrated electrons would heal inactive Fe(III) species faster and more effectively. Continuous Fe(II) recovery ensured Fe²⁺-based AOPs could proceed continuously.

4. Conclusion

A novel multichannel healing strategy based on TiO₂-CDs-FeOOH has been successfully constructed in order to response structural damage faster and more effectively during Fe²⁺-catalyzed AOPs. This ingenious hierarchical materials exhibits an extremely high pollutants degradation efficiency and long-term catalytic stability. TC degradation was completed within 3 min at a rate constant of $7.72 \times 10^{-1} \text{ min}^{-1}$. Based on the combined results of optical and electrochemical properties, we demonstrated that multiple electron transfer led to highly efficient interfacial charge separation and fast healing of Fe(II), which enhanced dramatically catalytic activity. In addition, the multiple-channels healing process was confirmed by SECM technique, and quantitatively studied the multiple electron transfer dynamics of the different interfaces, providing deep-seated synergic mechanism. This work offers a promising approach for achieving high-efficiency regeneration of the active Fe(II) species for persistent H₂O₂ decomposition in environmental remediation.

Conflict of interest

The authors declare no conflict of interest.

Acknowledgements

This research work was financially supported by National Natural Science Foundation of China (Grant Nos. 21327005, 21575115, and 21705117); the Program for Chang Jiang Scholars and Innovative Research Team, Ministry of Education, China. (Grant No. IRT-16R61); the Program of Innovation and Entrepreneurial for Talent, Lan Zhou, Gansu Province, China (Grant No. 2014-RC-39).

Appendix A. Supplementary data

Supplementary material related to this article can be found, in the online version, at doi:<https://doi.org/10.1016/j.apcatb.2019.03.033>.

References

- [1] E. Brillas, I. Sirés, M.A. Oturan, Chem. Rev. 109 (2009) 6570–6631.
- [2] N.N. Tušar, D. Maučec, M. Rangus, I. Arčon, M. Mazaj, M. Cotman, A. Pintar, V. Kaučič, Adv. Funct. Mater. 22 (2012) 820–826.
- [3] C.C. Wang, J.R. Li, X.L. Lv, Y.Q. Zhang, G. Guo, Energy Environ. Sci. 7 (2014) 2831–2867.
- [4] Q. Ma, H. Zhang, X. Zhang, B. Li, R. Guo, Q. Cheng, X. Cheng, Chem. Eng. J. (2018), <https://doi.org/10.1016/j.cej.2018.12.036>.
- [5] M. Zhang, X. Xie, M. Tang, C.S. Criddle, Y. Cui, S.X. Wang, Nat. Commun. 4 (2013) 1866.
- [6] M. Xing, W. Xu, C. Dong, Y. Bai, J. Zeng, Y. Zhou, J. Zhang, Y. Yin, Chem 4 (2018) 1359.
- [7] A.L.T. Pham, F.M. Doyle, D.L. Sedlak, Water Res. 46 (2012) 6454–6462.
- [8] G. Subramanian, G. Madras, Chem. Commun. 53 (2017) 1136–1139.
- [9] A. De Luca, R.F. Dantas, S. Esplugas, Appl. Catal. B: Environ. 179 (2015) 372–379.
- [10] T. Li, Z. Zhao, Q. Wang, P. Xie, J. Ma, Water Res. 105 (2016) 479–486.
- [11] L. Chen, J. Ma, X. Li, J. Zhang, J. Fang, Y. Guan, P. Xie, Environ. Sci. Technol. 45 (2011) 3925–3930.
- [12] Y. Qin, F. Song, Z. Ai, P. Zhang, L. Zhang, Environ. Sci. Technol. 49 (2015) 7948–7956.
- [13] C. Jiang, S. Garg, T.D. Waite, Environ. Sci. Technol. 49 (2015) 14076–14084.
- [14] G. Zhang, Z. Wu, H. Liu, Q. Ji, J. Qu, J. Li, Small 13 (2017) 1702225.
- [15] B. Zhang, L. Wang, Y. Zhang, Y. Ding, Y. Bi, Angew. Chem. Int. Ed. 57 (2018) 2248–2252.
- [16] D. Zheng, X.N. Cao, X. Wang, Angew. Chem. Int. Ed. 55 (2016) 11512–11516.
- [17] M. Xing, B. Qiu, M. Du, Q. Zhu, L. Wang, J. Zhang, Adv. Funct. Mater. 27 (2017) 1702624.
- [18] B. Qiu, M. Xing, J. Zhang, J. Mater. Chem. A 3 (2015) 12820–12827.
- [19] T. Xu, R. Zhu, G. Zhu, J. Zhu, X. Liang, Y. Zhu, H. He, Appl. Catal. B: Environ. 212 (2017) 50–58.
- [20] S. Qu, X. Wang, Q. Lu, X. Liu, L. Wang, Angew. Chem. Int. Ed. 51 (2012) 12215–12218.
- [21] W. Stöber, A. Fink, E. Bohn, J. Colloid Inter. Sci. 26 (1968) 62–69.
- [22] D. Du, W. Shi, L. Wang, J. Zhang, Appl. Catal. B: Environ. 200 (2017) 484–492.
- [23] X. Ning, L. Ma, S. Zhang, D. Qin, D. Shan, Y. Hu, X. Lu, J. Phys. Chem. C 120 (2016) 919–926.
- [24] X. Ning, W. Li, Y. Meng, D. Qing, J. Chen, X. Mao, Z. Xue, D. D. Shan, S. Devaramani, X. Lu, Small 14 (2018) 1703989.
- [25] H. Xia, D. Qin, X. Zhou, X. Liu, X. Lu, J. Phys. Chem. C 117 (2013) 23522–23528.
- [26] L. Ge, K. Moor, B. Zhang, Y. He, J.-H. Kim, Nanoscale 6 (2014) 13579–13585.
- [27] A.E. Harvey, J.A. Smart, E.S. Amis, Anal. Chem. 27 (1955) 26–29.
- [28] S.M. Hao, J. Qu, Z.S. Zhu, X.Y. Zhang, Q.Q. Wang, Z.Z. Yu, Adv. Funct. Mater. 26 (2016) 7334–7342.
- [29] H. Yu, R. Shi, Y. Zhao, G. Waterhouse, L. Wu, C. Tung, T. Zhang, Adv. Mater. 28 (2016) 9454–9477.
- [30] W. Shi, F. Guo, H. Wang, M. Han, H. Li, S. Yuan, H. Huang, Y. Liu, Z. Kang, Appl. Catal. B: Environ. 219 (2017) 36–44.
- [31] P. Zhang, T. Wang, X. Chang, L. Zhang, J. Gong, Angew. Chem. Int. Ed. 55 (2016) 5851–5855.
- [32] H. Yu, Y. Zhao, C. Zhou, L. Shang, Y. Peng, Y. Cao, L.Z. Wu, C.H. Tung, T. Zhang, J. Mater. Chem. A 2 (2014) 3344–3351.
- [33] Q. Liu, T. Chen, Y. Guo, Z. Zhang, X. Fang, Appl. Catal. B: Environ. 205 (2017) 173–181.
- [34] J. Zhang, Z. Yu, Z. Gao, H. Ge, S. Zhao, C. Chen, S. Chen, X. Tong, M. Wang, Z. Zheng, Y. Qin, Angew. Chem. Int. Ed. 56 (2017) 816–820.
- [35] Y. Li, Z. Liu, Y. Wu, J. Chen, J. Zhao, F. Jin, P. Na, Appl. Catal. B: Environ. 224 (2018) 508–517.
- [36] X. Shi, M. Fujitsuka, Z. Lou, P. Zhang, T. Majima, J. Mater. Chem. A 5 (2017) 9671–9681.
- [37] J. Feng, H. Xu, Y. Dong, S. Ye, Y. Tong, G. Li, Angew. Chem. Int. Ed. 55 (2016) 3694–3698.

- [38] Z. Wang, W. Wu, Q. Xu, G. Li, S. Liu, X. Jia, Y. Qin, Z.L. Wang, *Nano Energy* 38 (2017) 518–525.
- [39] M. Liu, X. Qiu, M. Miyauchi, K. Hashimoto, *J. Am. Chem. Soc.* 135 (2013) 10064–10072.
- [40] H. Yu, H. Irie, Y. Shimodaira, Y. Hosogi, Y. Kuroda, M. Miyauchi, K. Hashimoto, *J. Phys. Chem. C* 114 (2010) 16481–16487.
- [41] B.C.M. Martindale, G.A.M. Hutton, C.A. Caputo, S. Prantl, R. Godin, J.R. Durrant, E. Reisner, *Angew. Chem. Int. Ed.* 56 (2017) 6459.
- [42] R. Shi, Z. Li, H. Yu, L. Shang, C. Zhou, G.I.N. Waterhouse, L. Wu, T. Zhang, *ChemSusChem* 10 (2017) 4650–4656.
- [43] J. Su, X. Feng, J.D. Sloppy, L. Guo, C.A. Grimes, *Nano Lett.* 11 (2011) 203–208.
- [44] J.S. Lee, D.H. Shin, J. Jang, *Energy Environ. Sci.* 8 (2015) 3030–3039.